

Probing stellar-mass primordial black holes with type Ia supernova microlensing

Mingqi Sun¹ and Kai Liao^{1*}

¹*School of Physics and Technology, Wuhan University, Wuhan 430072, China*

(Dated: March 31, 2025)

Gravitationally lensed quasars have served as a powerful tool for studying the composition of dark matter (DM) in lensing galaxies. In this work, we propose a novel method to investigate stellar-mass primordial black holes (PBHs) by using the microlensing effect of strongly lensed Type Ia supernovae (SNe Ia). Using the parameters of the lensed quasar system PG 1115+80, such as convergence, shear, and stellar/dark matter fractions, we generate microlensing magnification maps. A uniform brightness disk model is applied to these maps to evaluate the microlensing amplitude at different stages of the supernova explosion. We extend this analysis by employing the strong lensing parameters derived from the Vera C. Rubin Observatory's Legacy Survey of Space and Time (LSST) to create extensive image datasets of lensed SNe Ia. Utilizing these datasets and the Kolmogorov-Smirnov (KS) test, we compare two models: (1) the fiducial model, where galaxies are composed of stars and smooth DM, and (2) the alternative model, where galaxies consist of stars and compact DM, specifically PBHs. Our preliminary analysis predicts that at least 60 image datasets are required to distinguish these two scenarios at a 95% confidence level. Additionally, by incorporating the *Strong Lensing Halo model-based mock catalogs (SL-Hammocks)*, which provide more realistic and precise image data, we refine our prediction to assess the data requirements for distinguishing cases where PBHs constitute fractions x of the total dark matter mass. Our findings indicate that 50, 55, and 65 image datasets, corresponding to compact dark matter fractions of 100%, 50%, and 25% (denoted by x), are necessary to distinguish between the specific models.

I. INTRODUCTION

Dark matter is a hypothetical form of matter that, on a cosmological scale, is approximately five times more abundant than the familiar baryonic matter, such as matter composed of neutrons and protons. On the scale of galaxies, dark matter accounts for about 80% of a galaxy's total mass. Since Zwicky's studies of galaxy clusters[1], astronomers have widely accepted the gravitational effects of dark matter and applied them extensively in astrophysical research. However, a solid theoretical understanding of the nature of dark matter remains lacking. Current research on dark matter models is primarily divided into two categories. One category involves particle dark matter, such as axions, weakly interacting massive particles (WIMPs), etc[2, 3], which are smoothly distributed. The other category considers dark matter in a more compact form, such as massive compact halo objects (MACHOs) and primordial black holes (PBHs)[1, 4]. Research into the nature of dark matter is crucial for the precise construction of cosmological models.

Microlensing is a vital tool for studying the composition of matter in galaxies. Analogous to lensed quasars, strongly lensed supernovae also produce multiple images. On this foundation, microlensing effects are primarily influenced by compact objects, such as stars distributed within the lens galaxies[5, 6]. Light from a source (e.g., a quasar[7] or supernova[8]) is further split into multiple sub-images by the microlensing effect. These sub-images typically have angular separations on the μ -arcseconds

scale, which is far below the spatial resolution limit of current telescopes. As a result, we can only infer the specific impact of microlensing by observing anomalies in the strongly lensed images, such as flux variations or time delays.

Current research indicates that typical microlensing signals primarily originate from the distribution of stars within the lens galaxy[9, 10]. However, studies on the light curves of lensed quasars suggest that incorporating compact objects, such as primordial black holes (PBHs), provides a more comprehensive explanation for the influence of microlensing effect on the light curves[11, 12]. A considerable amount of research has utilized galactic microlensing to constrain the abundance of primordial black holes (PBHs) across various mass ranges, such as[13].

The angular size of a Type Ia supernova is comparable to that of typical Einstein radii of stars in lensing galaxies. This naturally leads to the idea of using supernovae as an alternative to lensed quasars for dark matter studies with microlensing. Compared to lensed quasars, supernovae present several significant advantages. First, the source size of Type Ia supernovae is more standardized, eliminating the need for complex considerations, such as those required in [14], when using SNe as the source in lensing systems. Second, as 'standard candles,' the unlensed flux of supernovae at each stage of their explosion is much more predictable. This predictability enables direct use of image flux to study the microlensing effect, rather than relying on flux ratios, as is necessary when quasars are chosen as the source. These advantages enhance the efficiency of statistical analyses[8]. Although the sample size of lensed supernovae has been relatively small in the past, limiting the ability to conduct statistical analysis, the next generation of telescopes, Vera C. Rubin Observatory[8] and Nancy Grace Roman Space

* E-mail:liaokai@whu.edu.cn

Telescope[15], is highly likely to address this issue, offering a significant increase in the number of detectable events. To be more specific, the Legacy Survey of Space and Time (LSST) from the Rubin Observatory will detect hundreds of SN Ia events per year[16, 17], which would significantly expand the sample size and enhance the statistical power of future analyses.

In this work, we use microlensing of type Ia supernovae to probe stellar-mass primordial black holes (PBHs). By modeling the lens galaxy and its stellar mass distribution, we can calculate the microlensing scatter in the usual manner. Assuming the extreme case where all dark matter consists of PBHs, we generate two scenarios: stars+smooth DM and stars+PBHs. In this context, predictions can be made regarding how many lensed supernova data points are needed to reject one of these cases.

The paper is structured as follows. In Section II, we refer to the parameters in a realistic lensed quasar system, PG 1115+80, to provide an initial look at lensed SN Ia and demonstrate how PBHs influence the microlensing scatter. In Section III, we simulate the entire lensing process to generate more simulated lensed SN Ia data, allowing us to make the predictions mentioned earlier. Finally, in Section IV, we will use the mock catalogs from the LSST study [18] to give a general discussion and then provide our conclusions in Section V.

II. THE EFFECT OF PBHS IN MICROLENSING

To study the microlensing effects caused by stars and other compact objects, we must first simulate the magnification map. This simulation of the magnification map is performed using the **MULES**¹ Python package. It is pixelated, with the magnification factor of each pixel calculated using a ray-tracing algorithm[20]. The spatial distribution of stars within the lensing galaxy is random, represented in our magnification map as randomly scattered points. Three parameters must be generated for microlensing simulation, κ , γ , f , representing the local environment in which the stars are situated. κ is the convergence, which is defined as a dimensionless surface density, while the γ is called shear and f is the compact matter fraction.

According to the review[8], to date, six lensed supernova events have been successfully observed. But none of them are typical lensing systems for the future survey like LSST. The data for lensed supernovae is so limited that we have to use the lensed quasar system, PG 1115+080, and simply replace the source from a quasar to our SN Ia, as this system has been well studied. The local environment for the 4 images had already been given[19],

which is showed in Table I. This section directly uses these parameters.

We simulate magnification maps for these four images using both (κ, γ, f^*) and $(\kappa, \gamma, f^* + f_{\text{PBHs}})$, where * stands for the stars. They are showed in Fig.1. We assume PBHs have the same mass of stars which is set to $\langle M_{\text{PBHs}} \rangle = \langle M_* \rangle = 0.3M_{\odot}$. The maps have a size of $20\langle R_{\text{Ein}} \rangle \times 20\langle R_{\text{Ein}} \rangle$ while the pixel resolution is 4096×4096 , $\langle R_{\text{Ein}} \rangle = 2.09 \times 10^{16}$ cm in the source plane, corresponding to redshift configuration ($z_s = 1.72$, $z_l = 0.31$). Here we use the following formula to calculate $\langle R_{\text{Ein}} \rangle$:

$$\langle R_{\text{Ein}} \rangle = \sqrt{\frac{4G\langle M_* \rangle D_s D_{\text{ls}}}{c^2 D_{\text{ls}}}}. \quad (1)$$

Throughout this work, the cosmological model is set to the flat Λ CDM with parameters $H_0 = 67.8 \text{ km s}^{-1} \text{ Mpc}^{-1}$, and $\Omega_m = 0.3$ [21], respectively.

This work uses a simple, expanding disk model to simulate the supernova explosion process, thereby obtaining the influence of microlensing on the luminosity of the supernova. According to [22], the microlensing effect is relatively sensitive to the average size of the source but does not exhibit a strong correlation with specific details in the source's profile model, such as spectral and luminosity distributions. Thus, we place a circular disk with a gradually increasing radius over the magnification map to simulate the supernova. By neglecting the luminosity model of the supernova, we assume that different positions on the disk contribute equally to the overall microlensing effect.

As an example, we randomly select a point on the magnification map to position the supernova, and we illustrate the variation of the microlensing effect as the disk expands in Fig.2. Here we show the microlensing effect using the parameter Δm ,

$$\Delta m = -2.5 \times \log_{10} \left| \frac{\mu}{\mu^{\text{SL}}} \right|, \quad (2)$$

$$\mu^{\text{SL}} = \frac{1}{(1 - \kappa)^2 - \gamma^2}, \quad (3)$$

μ is the total magnification, μ^{SL} is the macro magnification, and Δm is the micro magnification, expressed

TABLE I. Table of parameters for simulation, the κ, γ, f is given by [19], we also assume that all dark matter in the lensing galaxy exists in the form of primordial black holes (PBHs), resulting in a compact mass fraction of $f \equiv 1$ in this scenario.

Map	Image A 1	Image A 2	Image B	Image C
κ	0.424	0.451	0.502	0.356
γ	0.491	0.626	0.811	0.315
$f = f^*$	0.259	0.263	0.331	0.203
$f = f^* + f_{\text{PBHs}}$	1.000	1.000	1.000	1.000

¹ This package is freely available at <https://github.com/gdobler/mules>.

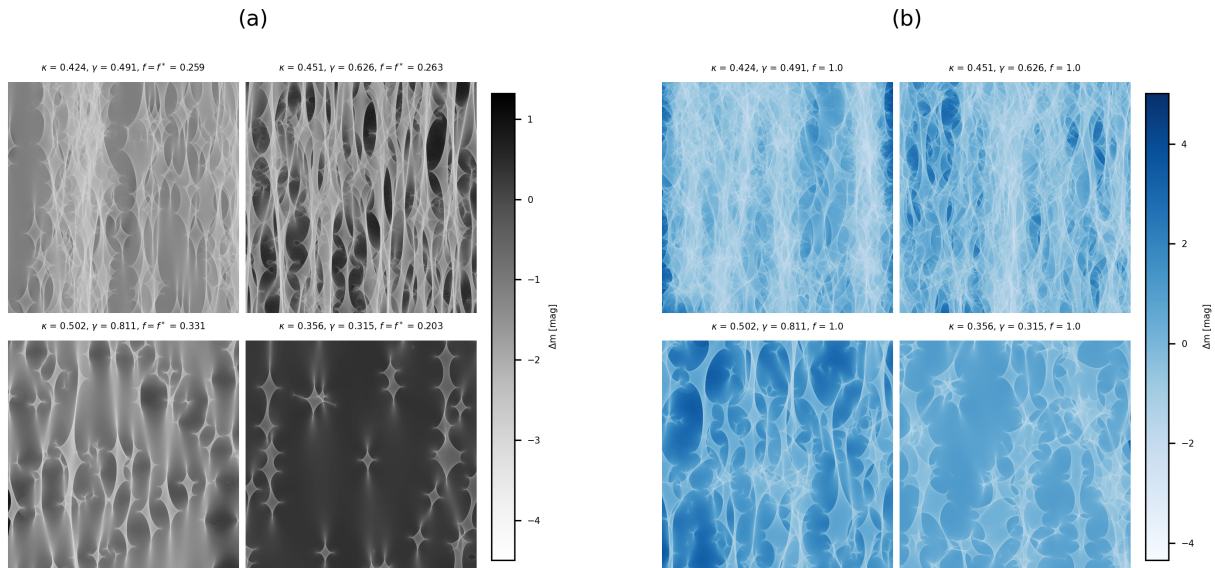


FIG. 1. Microlensing magnification maps, image (a) represents the stars and smooth DM model, the κ, γ, f comes from the study of PG 1115+080 [19], while image (b) represents the stars and PBHs model, we simply set $f \equiv 1$ for that. Both (a) and (b) includes 4 maps corresponding to 4 images of lensed supernova Ia. Every single map gets 4096 pixels each side, equal to $20(R_{\text{Ein}})$, per pixel have 1.02×10^4 cm in physical scale. The color gradient, from deep to light, corresponds to the magnitude of the microlensing effect as defined in equation 2.

in units of magnitude. The rate of exploration is set to 1.5×10^7 m/s, which is the average rate by [23]. We randomly place 20,000 disks representing the supernova, each corresponding to a size 30 days after the explosion, on the magnification map. This allows us to statistically analyze the distribution of the microlensing effect on the supernova explosion. Every single map have different distribution, they all showed in Fig.3. As we can see, two different models, stars with smooth dark matter and stars with PBHs, do have different distribution in each map. In the following sections of this article, we will present a quantitative study of this difference from a statistical perspective.

III. SIMULATE THE LENSED SNE IA

The basic equation in this work is as follows:

$$\Delta m = -2.5 \times \log_{10} |\mu^{\text{ML}}|, \quad (4)$$

where

$$\mu^{\text{ML}} = \frac{F^{\text{obs}}}{F^{\text{UnL}} \mu^{\text{SL}}}, \quad (5)$$

The F^{obs} corresponds to the observed flux result, while F^{UnL} represents the unlensed brightness of the type Ia supernova. μ^{SL} denotes the macro magnification. Using equation 4, the combination of these observables allows us to calculate the microlensing effect.

In this work, we aim to determine whether the inclusion of primordial black holes (PBHs) is necessary to account for additional microlensing effects. To do this, we require both Δm_{sim} and Δm_{obs} . The value of Δm_{sim} represents the microlensing magnification, in magnitudes, derived from our simulations. We generate a distribution for Δm_{sim} using the method outlined in section II. On the other hand, Δm_{obs} corresponds to the magnification observed directly. Ideally, we would obtain this value from actual observations, but since such data are not yet available, we instead randomly select values from the Δm_{sim} distribution to represent Δm_{obs} , while accounting for Gaussian random errors, denoted as σ_{others} (see subsection B).

Since Δm_{sim} is a distribution, whereas Δm_{obs} is a direct value, they cannot be directly compared. Thus, we require a probability-related quantity to quantify the difference between the two. The method for achieving this will be fully explained in the subsequent sections.

In the remainder of this article, we will consider the following two models:

a. Fiducial Model We consider the scenario where galaxies are composed of stars and smooth DM to generate both Δm_{sim} and Δm_{obs} . This model is used to validate whether our method is accurate.

b. Alternative Model We consider the scenario where galaxies are composed of stars and smooth DM to generate Δm_{sim} , while Δm_{obs} is generated assuming galaxies are composed of stars and PBHs. This model

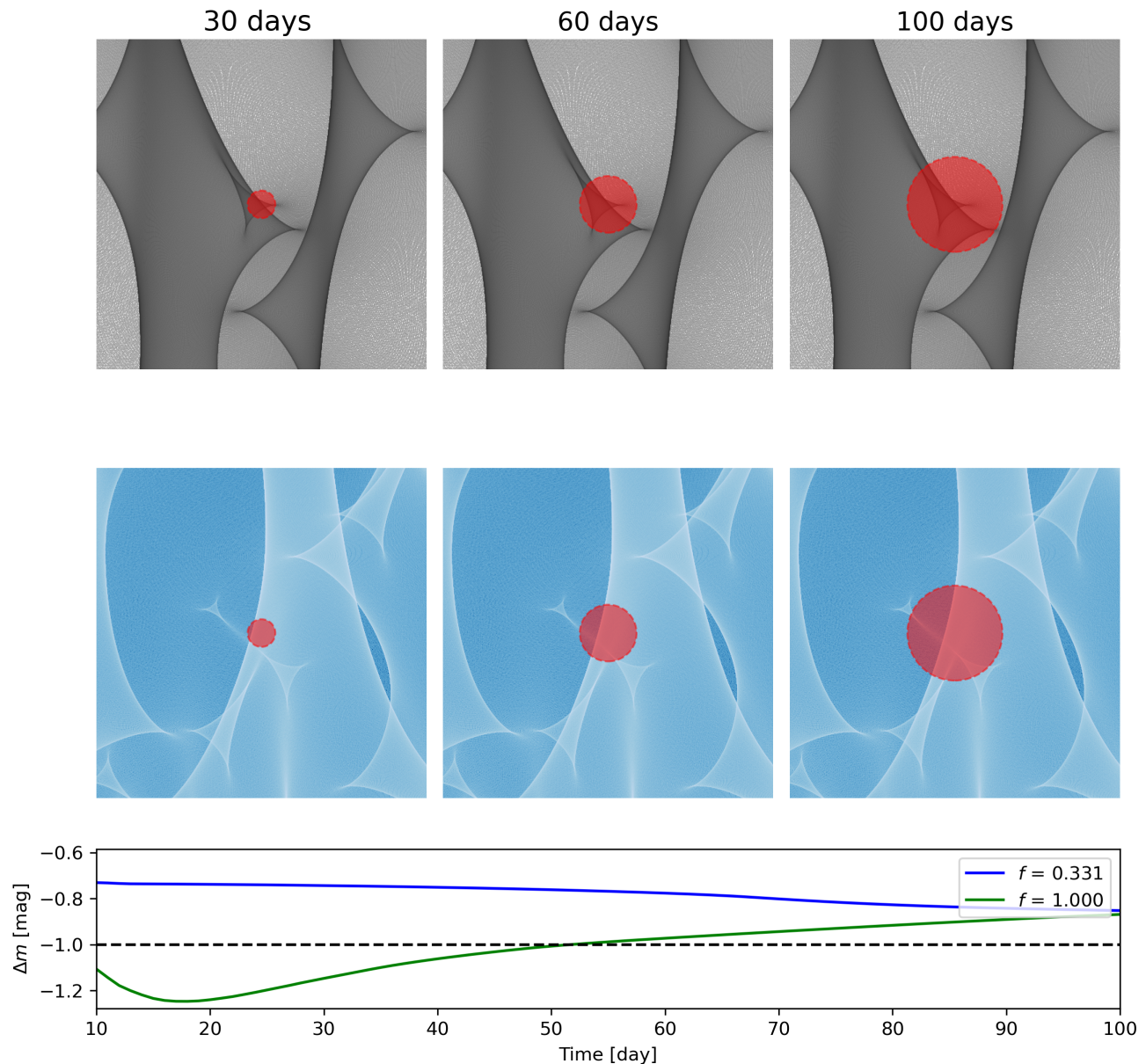


FIG. 2. The magnification map’s zoomed-in view displays an area of 1200×1200 pixels within the magnification map. As the SN Ia profile expands, the magnification values corresponding to the included pixel points within the profile are summed and averaged, therefore, the microlensing perturbation varies over time, as illustrated in the image at the bottom. The gray magnification map and the blue magnification map correspond to different scenarios: stars with smooth DM and stars with PBHs.

represents the central focus of this study.

A. Strong lensing process

This section is structured as follows. First, we provide a detailed description of how the dataset required for this study is generated. Second, we thoroughly describe the method used to statistically distinguish between the two models mentioned above. Finally we will directly show our result in the last subsection.

The upcoming LSST survey is expected to discover numerous lensed SNe Ia events, its observation strategy had already been studied by [24]. In this section, we select the mean values from the provided parameter distributions as the parameters for our strong lensing simulation to generate the local environment, (κ, γ, f) .

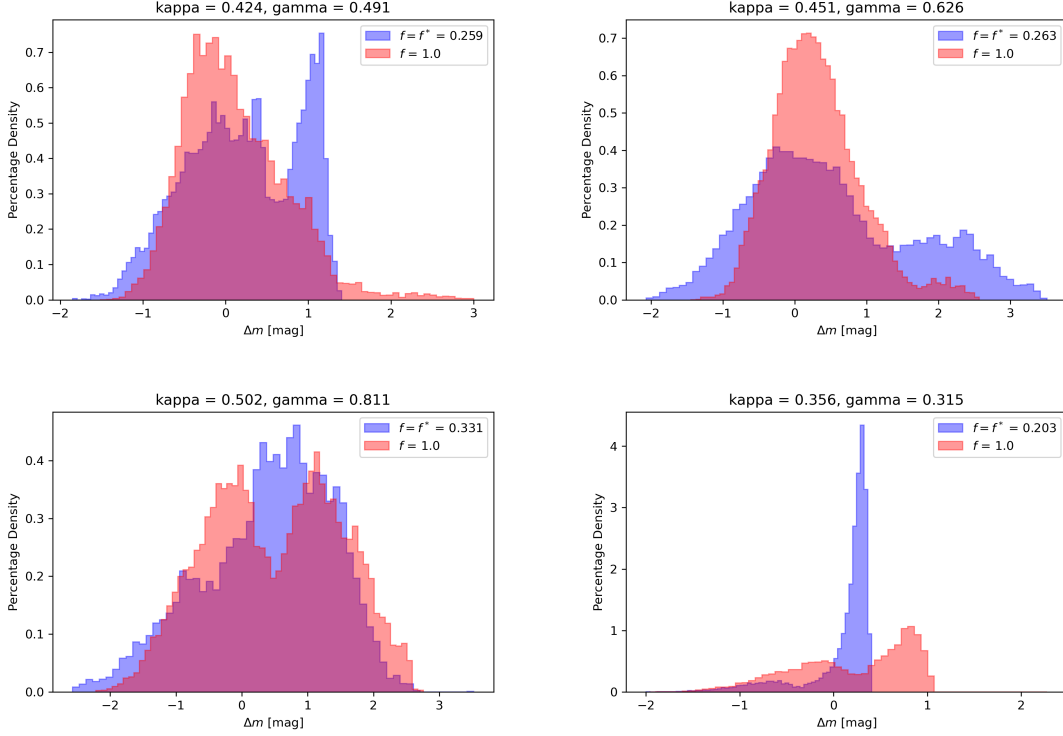


FIG. 3. Based on our assumptions for PG 1115+080, the histogram of the frequency distribution of the total magnification rates (measured in magnitudes) for the simulated 20000 microlensed supernova events is presented. The definition of the variable on the horizontal axis is provided in 2, reflecting the deviation of the microlensing magnification from the macro-magnification.

Here we use the Python package **Lenstronomy**[25]² to obtain these three parameters.

We simply set the mass model of the lensing galaxy as a power-law elliptic distribution, with its two-dimensional surface mass density distribution given by:

$$\kappa(x, y) = \frac{3-s}{2} \left(\frac{\theta_E}{\sqrt{q_{\text{lens}}x^2 + y^2/q_{\text{lens}}}} \right)^{s-1}, \quad (6)$$

while the q_{lens} is the axis ratio of the lens, s corresponds to the profile slope, and θ_E denotes the Einstein ring in arcseconds. The origin of the coordinate system is set at the center of the lens, with a rotation angle of ϕ_e (external shear is ignored in this work). In this subsection, we set these parameters as follows: $z_1 = 0.34$, $z_s = 0.80$, $q_{\text{lens}} = 0.7$, $s = 2.0$, $\theta_E = 0.44''$, $\phi_e = 65^\circ$, $\gamma_{\text{ext}} = 0$, which are all given by [24].

To generate multiple strongly lensed supernova events, we uniformly select a certain number of positions to place the supernovae (in the strong lensing simulation, the host

galaxy is neglected, and the supernova is treated as a point source). We then use the aforementioned Python package to calculate the image positions corresponding to each source location and display them in Fig.4.

According to equation 6 and the images' positions just calculated, the κ and γ can be rapidly worked out. The next step is to calculate the compact mass fraction, here we assume de Vaucouleurs profile[26]:

$$\kappa^*(x, y) = Ae^{-k(r/R_{\text{eff}})^{1/4}}, \quad (7)$$

which the corresponding complete expression is:

$$f^* = \frac{\kappa^*}{\kappa}. \quad (8)$$

Parameters in equation 7 are as follows: $k = 7.67$ [26], $r = \sqrt{q_{\text{lens}}x^2 + y^2/q_{\text{lens}}}$ is the position of the SN image relative to the coordinate origin, R_{eff} is effective radius of lens, A is the normalization factor. The effective radius R_{eff} of lens galaxy determined by the following equation,

$$\langle \Gamma \rangle = \Gamma_0 + \alpha(\lg(\theta_E/R_{\text{eff}}) + 0.05) + \beta(z_1 - 0.52). \quad (9)$$

According to [27], the lens galaxy's mass density gradient is $\langle \Gamma \rangle \approx 2.00$, and the values of the other parameters are $\Gamma_0 = 1.981_{-0.024}^{+0.024}$, $\alpha = 0.194_{-0.083}^{+0.092}$, and

² The official site is <https://github.com/lenstronomy>

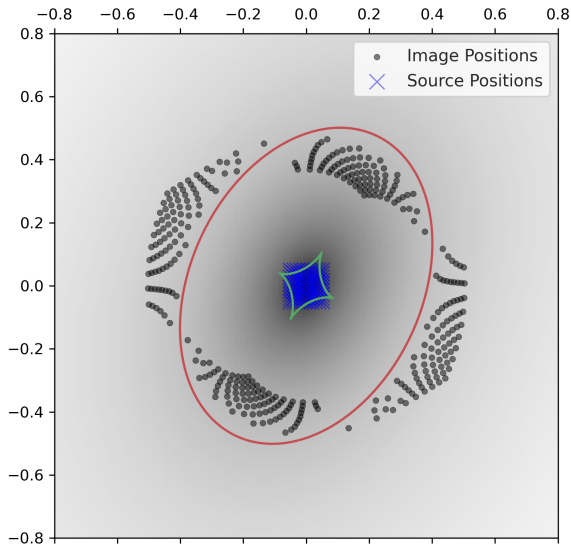


FIG. 4. A schematic diagram of the strong lensing process. The size of the diagram is $1.6'' \times 1.6''$, with the background color transitioning from light to dark corresponding to the convergence κ , from low to high. The red and green solid lines correspond to the critical line and caustic line of the strong lensing. The blue crosses and black circles represent the positions of the source and its images, respectively.

$\beta = -0.309^{+0.166}_{-0.160}$. For any given position, $\kappa_* \neq \kappa$ and what we want in this work is to identify the differences between the two scenarios mentioned previously, so f^* needs to be minimized as much as possible. Based on these conditions, we can determine value of the normalization factor A , thereby obtaining the expression for f^* .

So far, the preparatory work for simulating μ^{SL} and Δm_{sim} has been completed. The final subsection of this section will provide a detailed discussion of the final simulation results.

B. Other errors

To ensure the highest level of realism in the simulation, a series of necessary errors need to be introduced when simulating the observed supernova magnitudes:

$$\sigma_{\text{others}} \sim \sqrt{\sigma_{\text{SL}}^2 + \sigma_{\text{int}}^2 + \sigma_{\text{pho}}^2}. \quad (10)$$

σ_{SL} represents the strong lensing error, originating from the process of modeling the lens. By assuming a scenario where microlensing can be ignored, we can fit the parameters of the strong lensing process, such as θ_{E} , q_{lens} , and s , as discussed in the previous subsection. This error arises directly from these parameter estimations. In this work, we approximate it as a constant: $\sigma_{\text{SL}} \approx 0.04$ mag.

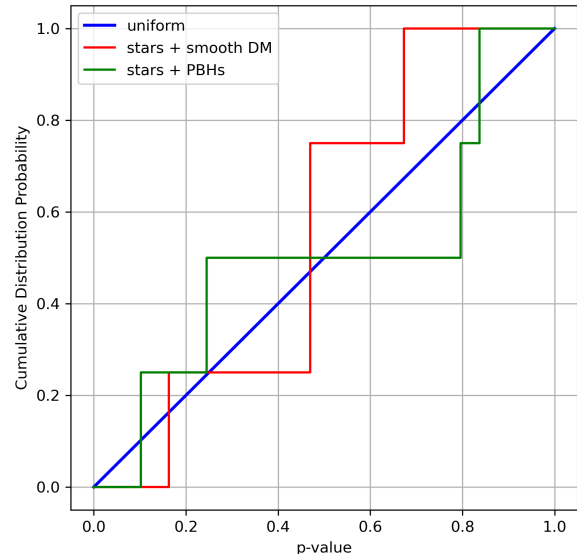


FIG. 5. The cumulative distribution function of p-values. The red and green solid lines correspond to the two models, stars with smooth DM and stars with PBHs, the blue line is uniform distribution. We performed a KS test using the CDFs of the two models, and the results indicate that both $p_{\text{KS}} > \alpha$. Therefore, based on the current sample size, we cannot reject the hypothesis H_0 in both models.

σ_{int} represents the intrinsic error, which arises from the variability in the intrinsic luminosity of SN Ia at a given redshift, z_s . According to [28, 29], we approximate it as: $\sigma_{\text{int}} \approx 0.15$ mag.

σ_{pho} represents the photometric error, which comes from the telescope used to detect the SN Ia. For instance, the flux detected by the telescope introduces some errors, and the redshift of SN Ia cannot be measured without uncertainty. Here, we approximate it as: $\sigma_{\text{pho}} \approx 0.01$ mag.

Considering all the above errors, we obtain $\sigma_{\text{others}} \approx 0.16$ mag, and we will use this value in the next subsection.

C. Method

After generating the Δm_{obs} and Δm_{sim} using the method we have mentioned above, an empirical measurement of the p-value can be used for our statistical analysis. Its form is as follows:

$$p = 2 \times \min\{P(\Delta m_{\text{sim}} > \Delta m_{\text{obs}}), P(\Delta m_{\text{sim}} < \Delta m_{\text{obs}})\}. \quad (11)$$

To statistically assess and test the dark matter models, we performed a Kolmogorov-Smirnov (KS) test [30] on the microlensing effects produced by the two models using the p-values defined in equation 11. When a hypothesis is true, the corresponding p-values are uniformly

distributed between 0 and 1³.

The reason for choosing the KS test over the chi-squared test is primarily that the chi-squared test performs poorly with small sample sizes, whereas the KS test remains sensitive even with limited samples. Here, we define null hypothesis: - H_0 : The true scenario is stars with smooth DM. But we use two different model, fiducial model-stars with smooth DM and alternative model-stars with PBHs, as Δm_{obs} to test this hypothesis.

The CDF (Cumulative Distribution Function) used in the KS test is shown in Fig.5. The KS test compares the separation between the CDFs of the two samples and a uniform distribution to calculate the p_{KS} . Once p_{KS} is obtained, it can be compared with the significance level α . For example, at a 95% confidence level, if $p_{\text{KS}} > \alpha = 0.05$, we conclude that we cannot reject the hypothesis at this confidence level.

As an example, we use the dataset containing four image data points introduced in Section II to provide a brief explanation. The results are $p_{\text{KS}} = 0.472 \gg 0.05$ and $p_{\text{KS}} = 0.405 \gg 0.05$. This indicates that, based on the four images in our assumption, we cannot statistically reject the null hypothesis. For the fiducial model (stars with PBHs), Δm_{obs} and Δm_{sim} come from the same distribution, making $p_{\text{KS}} > 0.05$ an inevitable result.

Thus, alternative model is what we need to focus on because determining whether it can be rejected is key to identifying which dark matter model is correct. In Section III, we will conduct further simulations to obtain the expected number of supernova events needed to distinguish between the two models.

D. Final results

After simulating the strong lensing process using the method described in section III A, we generated numerous parameter pairs, (κ, γ, f^*) , corresponding to different SN Ia events. We use these parameters to produce various magnification maps and calculate Δm_{sim} of 30, 60, 100 days after the explosion, following the previously mentioned method, then generate p-values using 11. Additionally, to make the simulation more realistic, we incorporate the error, σ_{others} , in our KS test.

We plotted the curve of the p_{KS} as a function of the number of magnification maps in Fig.6. For each number of maps, we perform the KS test 100 times and use the median value as our data point. From the plot, it can be observed that for alternative model, although the p_{KS} exhibits significant fluctuations initially, it shows an overall decreasing trend. This indicates that as the amount of statistical data increases, the p_{KS} generated by the KS test decreases significantly (as expected, since the data used for the p-value in alternative model originates from

different models). For the fiducial model, the p_{KS} values consistently fluctuate around 0.5, regardless of the number of data points. This indirectly demonstrates the validity of our method.

The plot also reveals that the microlensing effects vary across supernovae at different stages of explosion, consistent with the results presented earlier in Fig.2. Moreover, even with this variability, it can be observed that for $N > 80$, the p_{KS} of each curve for alternative model consistently stabilizes below 0.05. This indicates that, based on the previously mentioned lens galaxy parameters and redshift configurations, it is expected to effectively distinguish between the two dark matter models, stars with smooth DM and stars with PBHs, after obtaining the p-value for 60 image data of lensed supernovae Ia at 30 days after explosion.

IV. REALISTIC PREDICTION

In the last section, we generated numerous image datasets of type Ia supernovae to provide input for our statistical tool—the KS test—in order to predict how much data is needed to distinguish whether dark matter is composed of smooth objects or 100% compact objects. However, the method used to produce these image data was not fully rigorous in terms of realistic observations, as each lensed supernova event has its own unique strong lensing parameters. Therefore, in this section, we will use mock catalogs from [18], which have simulated quasars and supernovae events that will be observed by LSST in the future. These catalogs are publicly available on the LSST Strong Lensing Science GitHub⁴.

The two main features of these mock catalogs are as follows. First, in contrast to similar mock catalogs like OM10 [16], these catalogs do not rely on simple mass models such as SIE (Singular Isothermal Ellipsoid) or PL (Power-Law) profiles. Instead, they provide a more detailed mass distribution that combines both dark matter and stellar components. This approach allows the simulations to consider not only galaxy-scale lenses but also group- and cluster-scale lenses. Second, the catalogs take into account the presence of subhalos and satellite galaxies, making the simulations more realistic and reliable.

After analyzing the simulation database, we selected 63 type Ia lensed supernova events from 240 predicted multiple-image lensed supernovae that could be observed by LSST. For each event, we removed the image near the lens center, and the type Ia multiple-image lensed supernova systems were then classified into two categories: double and quad systems. We plot the redshift data and Einstein radii of these systems in the Fig.7 and Fig.8.

³ Proof: <https://statproofbook.github.io/P/pval-h0>.

⁴ The official site is https://github.com/LSST-strong-lensing/data_public.

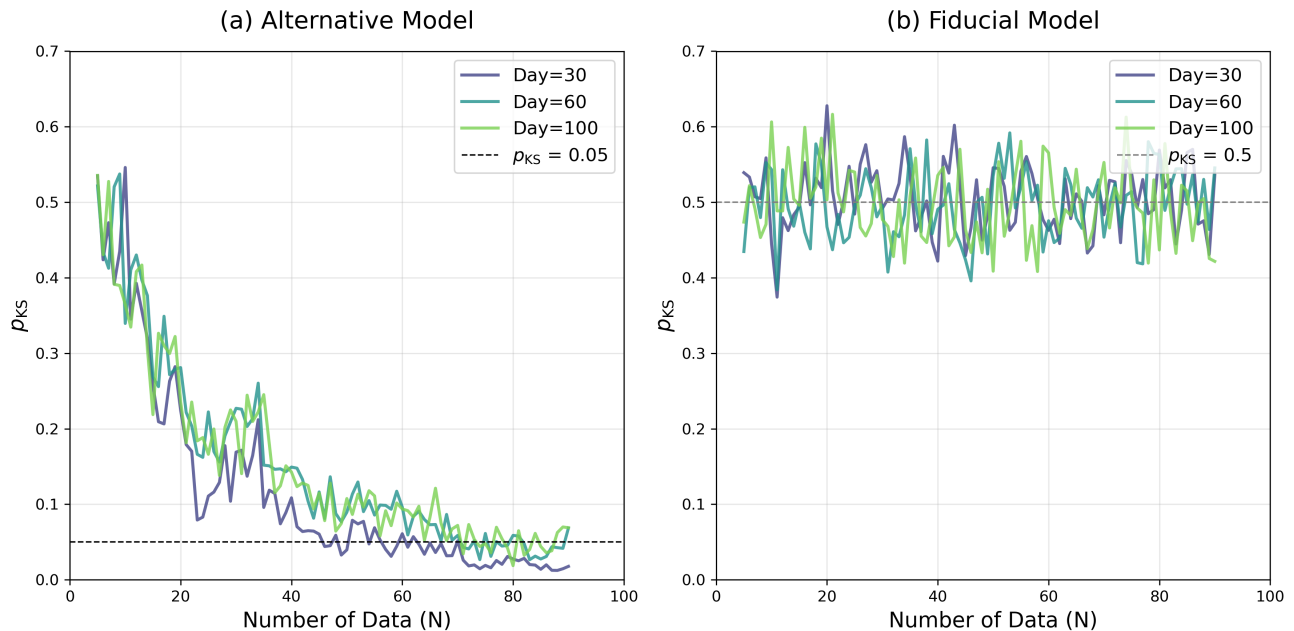


FIG. 6. The horizontal axis in the plot represents the number of magnification maps used for the KS test, while the vertical axis corresponds to the associated p_{KS} . For a given number of magnification maps, we perform 100 KS tests and select the median value. Both (a) and (b) show the p_{KS} curves for three different stages after the explosion. In (a), which corresponds to the alternative model, we observe that as the number of data points increases to 60, the p_{KS} values for all stages drop below 0.05. In (b), the p_{KS} values consistently fluctuate around 0.5. These results indicate that the alternative model allows us to reject the null hypothesis after obtaining 60 image data points. However, using the fiducial model, we can never reject the null hypothesis because, in this model, Δm_{obs} and Δm_{sim} actually originate from the same distribution.

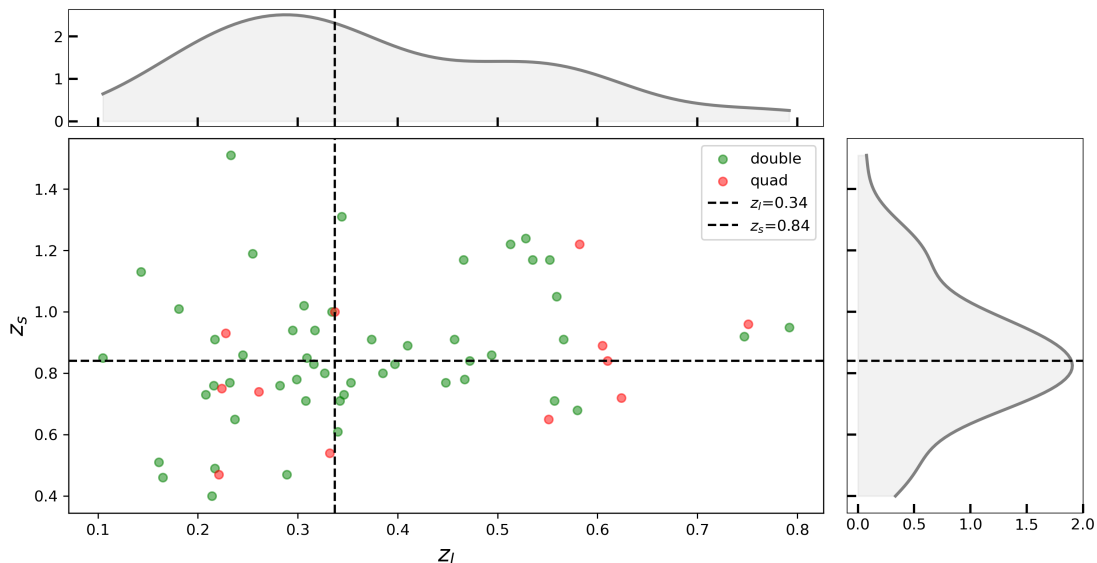


FIG. 7. The redshift distribution of lensed supernovae Ia is depicted in the plot, with green and red dots representing double and quad systems, respectively. The black dashed lines in the horizontal and vertical directions indicate the median values of the lens and source redshift distributions. Additionally, the upper and right margins of the plot display the fitted density functions for the marginal redshift distributions, providing a clearer view of the distribution trends.

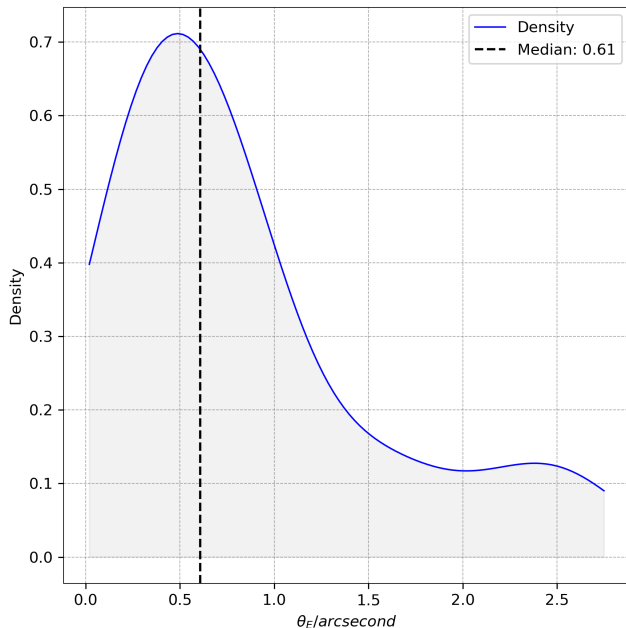


FIG. 8. The probability density curve of the Einstein radius distribution, fitted using a Gaussian kernel function, is applied to the selected data. The black dashed line represents the median of the Einstein radius distribution.

What’s more, the parameters of the local environment are also included in the mock catalogs mentioned above. These are all shown in Fig.9.

According to section III D, we can distinguish between the two dark matter models using data from 60 images, which correspond to 30 SN Ia events in the case of doubles or 15 SN Ia events in the case of quads. However, as mentioned earlier, there are 63 type Ia lensed supernova events available for analysis, meaning it is more than sufficient in realistic observational scenarios to differentiate between stars with smooth DM and stars with PBHs. In the second model, we assumed that all dark matter consists of compact objects ($f = f^* + f_{\text{PBHs}} \equiv 1$), which represents an extremely limiting assumption, as opposed to considering a mixture of smooth DM and PBHs. Given the extensive database provided by the chosen catalogs, more detailed and nuanced analyses can be conducted.

Here, we assume that the fraction of compact dark matter relative to the total dark matter is x . The compact matter fraction can then be described by the following equation:

$$f = f^* + x(1 - f^*), \quad (12)$$

where f^* corresponds to the scenario of stars with smooth DM.

Due to the limitations of computational power on personal computers, we temporarily refrain from performing a detailed numerical simulation for the precise values of x . Instead, we select three representative values: 1.0, 0.5, and 0.25, corresponding to compact dark matter making up 100%, 50%, and 25% of the total dark

matter mass, respectively, for preliminary calculations. Using the method described in Section III D and denote, we can redefine alternative model as : Δm_{obs} comes from the stars with x fraction of PBHs, incorporating all possible errors as detailed in Section III B. The final results are presented in Fig.10(here we only use alternative model). As we can see in Fig.6, using different disk sizes for the explosion at various days has little effect on our results when performing the KS test. Therefore, we use the size of 30 days after the explosion for our simulation in Fig.10.

From Fig.10, we can see that as the fraction of compact dark matter (x) decreases, more image data is required to reject the hypothesis we proposed, with the required numbers being 50, 55, and 65, respectively. When $x = 1.0$, the required number of image data differs from the 60 data points needed in section III. This indicates that the precision of the model has a significant impact on the statistical results.

V. DISCUSSION

In this section, we will review some of the assumptions made in the simulations presented in this paper, analyze and discuss the results obtained. We will also point out areas for improvement, as well as aspects that need more detailed study in future simulations and observations.

As mentioned in section II, we assume that each part of the supernova explosion is equally affected by the microlensing effect because microlensing is particularly sensitive to the source size rather than the spectral or brightness distribution. Additionally, we have set the average velocity of SNe Ia to 1.5×10^7 m/s. It is important to note that when using lensed quasars to estimate the stellar-mass PBHs in lens galaxies, as in [14], the uncertainty in the source size has significant adverse effects. This is because the amplitude of microlensing variations decreases as the source size increases [31]. However, the situation is considerably different when using lensed SNe Ia. While the uncertainty in the explosion velocity can also influence the disk size on the magnification map when calculating microlensing scattering, Fig. 6 demonstrates that different explosion stages (corresponding to varying disk sizes) have minimal impact on the KS test results. As shown in the figure, all p_{KS} -curves for the various stages stabilize below 0.05 once the number of image data reaches 60. And this value of the velocity of explosion is much larger than any other velocity like the lens and the source, the velocity of the observer, and the proper motions of the microlenses[32], for example, the transverse velocity of lensed quasar is 600 km/s.

We have considered many potential errors in real observations in section III, but some aspects were overlooked. σ_{SL} is an error strongly correlated with the uncertainty of strong lensing parameters, such as redshifts (z_s, z_l), Einstein radii (θ_E), and source positions. Whether we can empirically treat this value as a constant is a topic that warrants further discussion in future studies. Similarly,

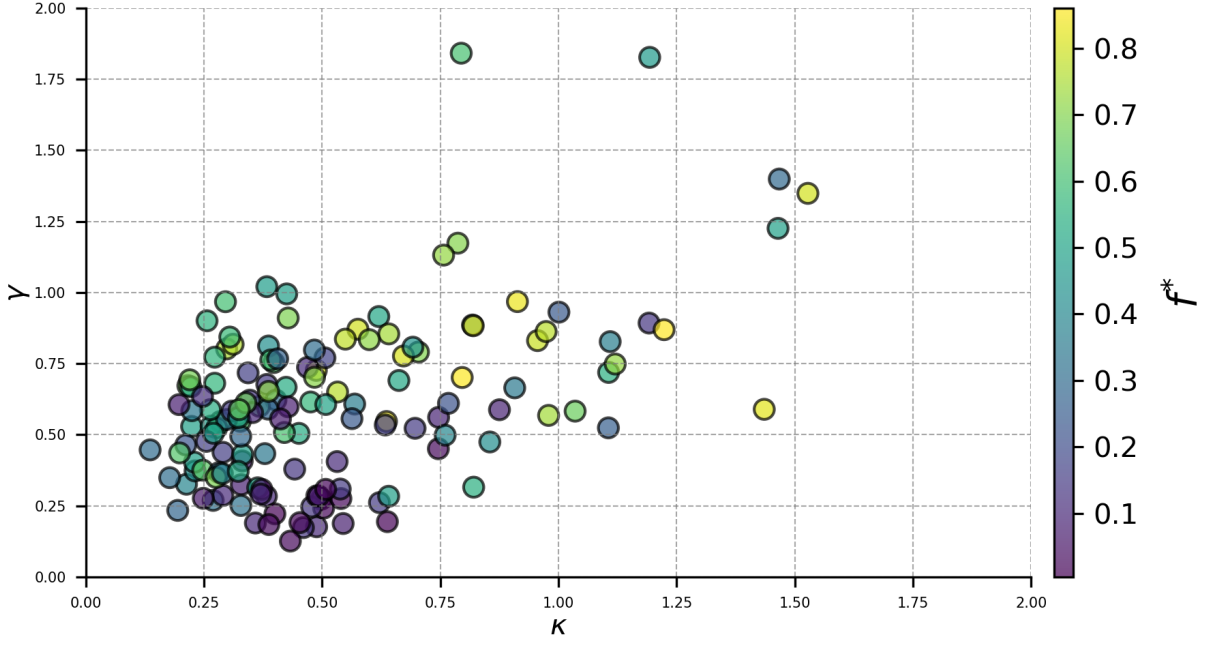


FIG. 9. The distribution of parameters, (κ, γ, f^*) . The horizontal and vertical axes correspond to κ (convergence) and γ (shear). The color of the data points represents the variation in f^* , which indicates the content of compact objects.

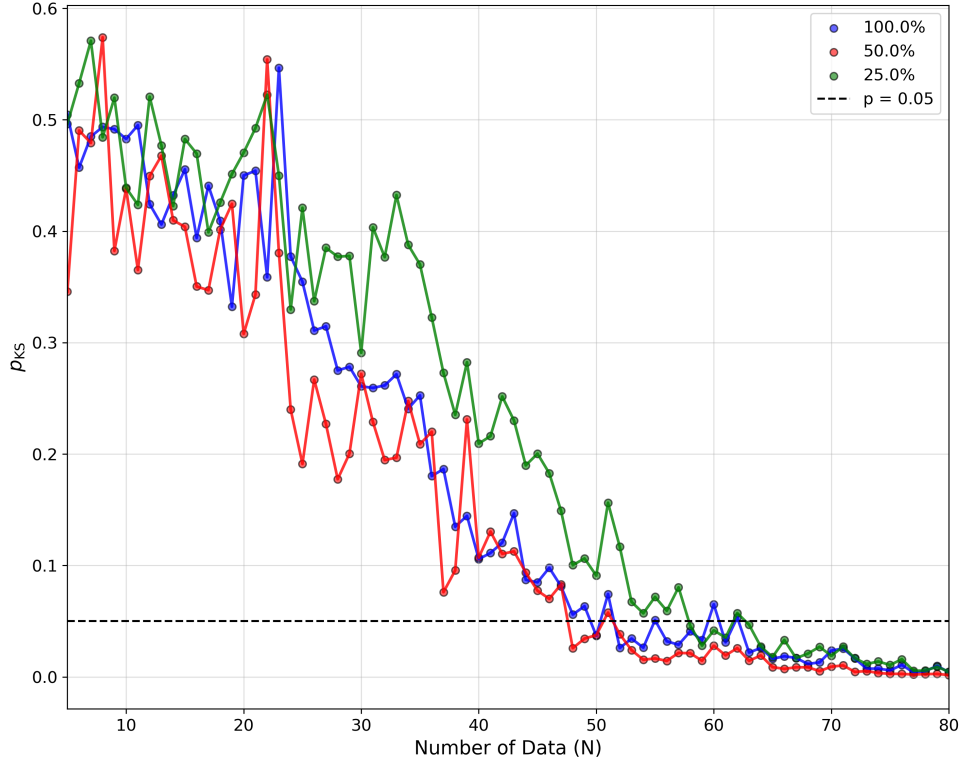


FIG. 10. The setup of the horizontal and vertical axes is consistent with that of Fig.6. The blue, red, and green curves correspond to different compact dark matter fractions. As in Fig.6, each data point represents the median value obtained after doing KS test 100 times.

σ_{int} and σ_{pho} require more specific evaluations based on different telescopes and surveys, such as LSST.

Another important issue to note is that, based on the statistical method we use, Δm_{obs} is randomly selected. Repeating the KS test multiple times to mitigate this randomness is essential. In this study, although we performed 100 tests for each data size (i.e., number of images), as shown in Fig. 10, the results still exhibit significant fluctuations. Increasing the number of tests in the future would greatly enhance the precision of the statistical results.

This work is inspired by the study of [14], which used the microlensing of lensed quasars to test whether the stars in the lensing galaxies of a population of lensed quasars are sufficient to account for the observed microlensing signal. The study concluded that, based on the current COSMOGRAIL sample, the two models—stars and smooth DM and stars and PBHs—cannot be distinguished. However, they predict that around 900 microlensing curves would be needed to distinguish between these two models. In contrast, for our work, this number is approximately 25 lensed SNe Ia events. Thanks to the upcoming LSST survey, approximately 3,500 lensed quasars and 200 lensed supernovae (including one-third being type Ia) with resolved multiple images will be discovered [18]. This means that in the future, we will have the opportunity to use both lensed QSOs and SNe Ia for real tests and detailed analyses, allowing us to study the fraction of compact objects relative to the total dark matter mass, using the realistic data from LSST.

VI. CONCLUSION

In this work, we study the microlensing effect caused by stellar-mass compact objects on lensed SNe Ia. More

specifically, we provide a statistical prediction for the amount of data required to study the content of stellar-mass PBHs in lensing galaxies. The main results are as follows:

a. Microlensing Effect By using the same image parameters (κ , γ , f), we can generally generate microlensing magnification maps. The histograms show that different scenarios exhibit visible differences, but these differences are not significant at a statistical level.

b. Preliminary Prediction By providing certain strong lensing parameters and varying the source position, we can quickly generate a large amount of image data for the KS test. We find that the two models can be distinguished after including 60 image data points, and different explosion stages have minimal influence on this result.

c. Realistic Prediction Using catalogs from the LSST's realistic studies, we assume different compact object fractions relative to the total dark matter mass as 100%, 50% and 25%. We find that approximately 50, 55 and 65 image data points are required to distinguish each of these scenarios, respectively.

Lensed SNe Ia are a powerful tool for studying the nature of dark matter in lensing galaxies. Although the article [33] finds no evidence of PBHs in the Milky Way, we cannot rule out the existence of PBHs in other galaxies. The best way to study this problem at cosmological distances is the method outlined in this paper.

ACKNOWLEDGMENTS

KL was supported by National Natural Science Foundation of China (No. 12222302) and National Key Research and Development Program of China (No. 2024YFC2207400).

-
- [1] G. Bertone and D. Hooper, History of dark matter, *Reviews of Modern Physics* **90**, 045002 (2018).
 - [2] A. Boyarsky, M. Drewes, T. Lasserre, S. Mertens, and O. Ruchayskiy, Sterile neutrino dark matter, *Progress in Particle and Nuclear Physics* **104**, 1 (2019).
 - [3] E. Oks, Brief review of recent advances in understanding dark matter and dark energy, *New Astronomy Reviews* **93**, 101632 (2021).
 - [4] C. Alcock, T. Axelrod, D. Bennett, K. Cook, H.-S. Park, K. Griest, S. Perlmutter, C. Stubbs, K. Freeman, B. Peterson, *et al.*, The search for massive compact halo objects with a (semi) robotic telescope, in *Robotic Telescopes in the 1990s*, Vol. 34 (1992) pp. 193–202.
 - [5] K. Chang and S. Refsdal, Flux variations of qso 0957+561 a, b and image splitting by stars near the light path, *Nature* **282**, 561 (1979).
 - [6] J. Gott III, Are heavy halos made of low mass stars—a gravitational lens test, *Astrophysical Journal*, Part 1, vol. 243, Jan. 1, 1981, p. 140-146. Research supported by the Alfred P. Sloan Foundation **243**, 140 (1981).
 - [7] G. Vernardos, D. Sluse, D. Pooley, R. Schmidt, M. Milon, L. Weisenbach, V. Motta, T. Anguita, P. Saha, M. O'Dowd, *et al.*, Microlensing of strongly lensed quasars, *Space Science Reviews* **220**, 14 (2024).
 - [8] S. H. Suyu, A. Goobar, T. Collett, A. More, and G. Vernardos, Strong gravitational lensing and microlensing of supernovae, *Space Science Reviews* **220**, 13 (2024).
 - [9] R. E. Schild, The time delay in the twin qso q0957+561, *Astronomical Journal* (ISSN 0004-6256), vol. 100, Dec. 1990, p. 1771-1776. **100**, 1771 (1990).
 - [10] E. E. Falco, J. Wambsganss, and P. Schneider, The role of microlensing in estimates of the relative time delay for the gravitational images of q0957+561, *Monthly Notices of the Royal Astronomical Society* **251**, 698 (1991).
 - [11] M. Hawkins, The signature of primordial black holes in the dark matter halos of galaxies, *Astronomy & Astrophysics* **633**, A107 (2020).
 - [12] M. Hawkins, Sdss j1004+4112: the case for a galaxy cluster dominated by primordial black holes, *Astronomy & Astrophysics* **643**, A10 (2020).

- [13] T. Blaineau, M. Moniez, C. Afonso, J.-N. Albert, R. Ansari, E. Aubourg, C. Coutures, J.-F. Glicenstein, B. Goldman, C. Hamadache, *et al.*, New limits from microlensing on galactic black holes in the mass range $10 m_{\odot} \leq m \leq 1000 m_{\odot}$, *Astronomy & Astrophysics* **664**, A106 (2022).
- [14] P. Awad, J. H. Chan, M. Millon, F. Courbin, and E. Paic, Probing compact dark matter objects with microlensing in gravitationally lensed quasars, *Astronomy & Astrophysics* **673**, A88 (2023).
- [15] J. Pierel, S. Rodney, G. Vernardos, M. Oguri, R. Kessler, and T. Anguita, Projected cosmological constraints from strongly lensed supernovae with the roman space telescope, *The Astrophysical Journal* **908**, 190 (2021).
- [16] M. Oguri and P. J. Marshall, Gravitationally lensed quasars and supernovae in future wide-field optical imaging surveys, *Monthly Notices of the Royal Astronomical Society* **405**, 2579 (2010).
- [17] D. A. Goldstein, P. E. Nugent, and A. Goobar, Rates and properties of supernovae strongly gravitationally lensed by elliptical galaxies in time-domain imaging surveys, *The Astrophysical Journal Supplement Series* **243**, 6 (2019).
- [18] K. T. Abe, M. Oguri, S. Birrer, N. Khadka, P. J. Marshall, C. Lemon, A. More, *et al.*, A halo model approach for mock catalogs of time-variable strong gravitational lenses, arXiv preprint arXiv:2411.07509 (2024).
- [19] G. C. Chen, C. D. Fassnacht, S. H. Suyu, C. E. Rusu, J. H. Chan, K. C. Wong, M. W. Auger, S. Hilbert, V. Bonvin, S. Birrer, *et al.*, A sharp view of h0licow: H₀ from three time-delay gravitational lens systems with adaptive optics imaging, *Monthly Notices of the Royal Astronomical Society* **490**, 1743 (2019).
- [20] R. Kayser, S. Refsdal, and R. Stabell, *Astrophysical applications of gravitational micro-lensing*, *Astronomy and Astrophysics (ISSN 0004-6361)*, vol. 166, no. 1-2, Sept. 1986, p. 36-52. Research supported by the Norges Almenvitenskapelige Forskningsrad. **166**, 36 (1986).
- [21] P. A. Ade, N. Aghanim, M. Arnaud, M. Ashdown, J. Aumont, C. Baccigalupi, A. Banday, R. Barreiro, J. Bartlett, N. Bartolo, *et al.*, Planck 2015 results-xiii. cosmological parameters, *Astronomy & Astrophysics* **594**, A13 (2016).
- [22] M. J. Mortonson, P. L. Schechter, and J. Wambsganss, Size is everything: universal features of quasar microlensing with extended sources, *The Astrophysical Journal* **628**, 594 (2005).
- [23] R. K. Sheth, M. Bernardi, P. L. Schechter, S. Burles, D. J. Eisenstein, D. P. Finkbeiner, J. Frieman, R. H. Lupton, D. J. Schlegel, M. Subbarao, *et al.*, The velocity dispersion function of early-type galaxies, *The Astrophysical Journal* **594**, 225 (2003).
- [24] N. Arendse, S. Dhawan, A. Sagués Carracedo, H. V. Peiris, A. Goobar, R. Wojtak, C. Alves, R. Biswas, S. Huber, S. Birrer, *et al.*, Detecting strongly lensed type ia supernovae with lsst, *Monthly Notices of the Royal Astronomical Society* **531**, 3509 (2024).
- [25] S. Birrer, A. J. Shajib, D. Gilman, A. Galan, J. Aalbers, M. Millon, R. Morgan, G. Pagano, J. W. Park, L. Teodori, *et al.*, lenstronomy ii: A gravitational lensing software ecosystem, arXiv preprint arXiv:2106.05976 (2021).
- [26] G. Dobler and C. R. Keeton, Microlensing of lensed supernovae, *The Astrophysical Journal* **653**, 1391 (2006).
- [27] R. Li, Y. Shu, and J. Wang, Strong-lensing measurement of the total-mass-density profile out to three effective radii for $z \approx 0.5$ early-type galaxies, *Monthly Notices of the Royal Astronomical Society* **480**, 431 (2018).
- [28] M. Betoule, R. Kessler, J. Guy, J. Mosher, D. Hardin, R. Biswas, P. Astier, P. El-Hage, M. König, S. Kuhlmann, *et al.*, Improved cosmological constraints from a joint analysis of the sdss-ii and snls supernova samples, *Astronomy & Astrophysics* **568**, A22 (2014).
- [29] D. M. Scolnic, D. Jones, A. Rest, Y. Pan, R. Chornock, R. Foley, M. Huber, R. Kessler, G. Narayan, A. Riess, *et al.*, The complete light-curve sample of spectroscopically confirmed sne ia from pan-starrs1 and cosmological constraints from the combined pantheon sample, *The Astrophysical Journal* **859**, 101 (2018).
- [30] I. M. Chakravarti, R. G. Laha, and J. Roy, *Handbook of methods of applied statistics*, Wiley Series in Probability and Mathematical Statistics (USA) eng (1967).
- [31] S. Refsdal and R. Stabell, Gravitational micro-lensing for large sources, *Astronomy and Astrophysics (ISSN 0004-6361)*, vol. 250, no. 1, Oct. 1991, p. 62-66. Research supported by NAF. **250**, 62 (1991).
- [32] M. Foxley-Marrable, T. E. Collett, G. Vernardos, D. A. Goldstein, and D. Bacon, The impact of microlensing on the standardization of strongly lensed type ia supernovae, *Monthly Notices of the Royal Astronomical Society* **478**, 5081 (2018).
- [33] P. Mróz, A. Udalski, M. K. Szymański, I. Soszyński, L. Wyrzykowski, P. Pietrukowicz, S. Kozłowski, R. Poleski, J. Skowron, D. Skowron, *et al.*, No massive black holes in the milky way halo, *Nature* **632**, 749 (2024).